Icarus 284 (2017) 206–215

Contents lists available at ScienceDirect

Icarus

journal homepage: www.elsevier.com/locate/icarus

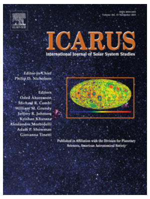

Dust in the arcs of Methone and Anthe

Kai-Lung Sun[a,*], Martin Seiß[a], M.M. Hedman[b], Frank Spahn[a]

[a] Institute for Physics and Astronomy, Karl-Liebknecht-Str. 24/25, 14476 Potsdam Golm, Germany
[b] Physics Department, University of Idaho, 875 Perimeter Drive, MS. 0903, Moscow ID 83844-0903, United States

ARTICLE INFO

Article history:
Received 4 May 2016
Accepted 8 November 2016
Available online 17 November 2016

Keywords:
Planetary rings
Saturn
rings
Saturn
satellites

ABSTRACT

Methone and Anthe are two tiny moons (with diameter $< 3\,\text{km}$) in the inner part of Saturn's E ring. Both moons are embedded in arcs of dust particles. To understand the amount of micron-sized dust in these arcs and their spatial distributions, we model the source, dynamical evolution, and sinks of the dust in the arc. We assume hypervelocity impacts of micrometeoroids on the moons produces these dust (Hedman et al., 2009), via the so called impact-ejecta process (Krivov et al., 2003; Spahn et al., 2006). After ejecting and escaping from the moons, these micron-sized particles are subject to several perturbing forces, including gravitational perturbation from Mimas, oblateness of Saturn, Lorentz force, solar radiation pressure, and plasma drag. Particles can be either confined in the arcs due to corotational resonance with Mimas, like their source moons (Cooper et al., 2008; El Moutamid et al., 2014; Hedman et al., 2009; Spitale et al., 2006), or pushed outward by plasma drag. Particle sinks are recollisions with the source moon, collisions with other moons, or migration out of the zone of interest. The erosion of particles due to plasma sputtering is also considered (Johnson et al., 2008), although its timescale is much larger than other sinks. Our simulation results show that ejecta from both moons can form maximal number densities between 10^{-4} and $10^{-3}\,\text{m}^{-3}$. In comparison with the observations of Anthe arc, the peak value in simulations is about an order of magnitude smaller. Plausible explanations for the difference include millimeter-sized particles as additional source and the uncertainties of impactor flux F_{imp} and the yields Y. The longitudinal extension of the Methone/Anthe arc in our simulation is 10.8°/15°, consistent with observations and theory (Hedman et al., 2009). Our results also show the lifetime distributions of particles and the heliotropic behavior of dust introduced by solar radiation pressure (Hedman et al., 2010a). The lifetimes of arc particles, defined by the time particles stay in the semi-major axes close to the source moons, are also related to particle size. Smaller ones ($< 5\,\mu\text{m}$) do not stay in the arc and instead migrate outward under the influence of plasma drag. Larger grains can stay in arc in the timescale of 100 years until they leave the arcs or collide with the source moons.

1. Introduction

Methone, Anthe, Pallene are three tiny moons located at the inner edge of Saturn's E ring, between the massive moons Mimas at $\sim 3.08\,R_s$ ($R_s = 60{,}268$ km is Saturn radius) and Enceladus at $\sim 3.95\,R_s$. Observations by the Cassini Imaging Science Subsystem (ISS) showed that dusty ring-arcs envelop the moons Methone and Anthe, and a torus exists in the vicinity of Pallene's orbit (Hedman et al., 2009). Although the mean radii of these moons are less than 3 km (Thomas et al., 2013), they are the most likely sources of these arcs through the impact-ejecta process, which produces dust ejecta caused by impacts of interplanetary micrometeoroids on these moons (Hedman et al., 2009; Krivov et al., 2003; Spahn et al., 2006). Due to the small size of the moons, ejecta can easily escape from the moons (Burns et al. 1999).

Methone's orbit is perturbed by both Mimas 15:14 corotation eccentricity resonance (CER) and Mimas 15:14 outer Lindblad resonance, while Anthe is perturbed by both Mimas 11:10 CER and Mimas 11:10 Lindblad resonance (Cooper et al., 2008; El Moutamid et al., 2014; Hedman et al., 2009; Spitale et al., 2006). The corotation resonances can trap dust particles released from the surface of these moons, leading to dust arcs in their vicinity. Theoretically, the maximal librating longitude is $360°/15 = 24°$ for the Methone arc, and $360°/11 \approx 32°$ for the Anthe arc. The observed length of the Methone arc is about 10°, while it is about 20° for Anthe (Hedman et al., 2009). An analog to the Anthe and Methone arcs is the Saturn's G ring arc, which is also confined in Mimas resonance and contains a tiny moon (Hedman et al., 2010b; 2009).

---

[*] Corresponding author.
E-mail address: akaronsun@gmail.com (K.-L. Sun).

http://dx.doi.org/10.1016/j.icarus.2016.11.009

If these arcs are similar to other faint rings like the Saturn G ring and are maintained by impact-ejecta process, then the arcs should contain significant amount of micron-sized particles. The small grain size implies that several perturbing forces shape these arcs simultaneously. For example, the interaction of solar radiation pressure, oblateness of Saturn, and Lorentz force can result in a heliotropic shape of the ring (an elliptic ring with *averaged* pericenter or apocenter in sun direction) as observed in the E ring (Hedman et al., 2012; Hamilton, 1993; Horányi et al., 1992) and the Charming ringlet in the Cassini Division (Hedman et al., 2010a). Another important perturbing force is plasma drag, which pushes E ring micron-sized particles outwards at a rate of order 1 R_s per Saturn year (Dikarev, 1999; Horányi et al., 2008).

This paper is organized as follows: We introduce our model including the impact-eject process, the dynamics, and the sinks of particles in Section 2. The simulation results are presented in Section 3, the brightness of arc in corotational frame of resonances, heliotropic behavior of particles, and the lifetime of arc materials. Discussions are given in Section 4.

2. Methods

To understand the spatial distribution and amount of dust near Methone and Anthe, we model the sources, dynamics, and sinks of dust. As proposed by Hedman et al. (2009), we assume dust to be produced through the impact-ejecta process (Krivov et al., 2003; Spahn et al., 2006), which is generated by the hypervelocity impacts of interplanetary dust on the surfaces of Methone and Anthe. The dynamics includes several perturbing forces that are summarized in Eq. (3). Finally, the major sink of dust are collisions with Methone/Anthe or Enceladus and outward migration induced by plasma drag. Erosion of particle by plasma sputtering is considered, although it requires much longer timescales than other sinks as shown later in Section 2.3 and Fig. 10.

2.1. Impact-ejecta process

A single hypervelocity impact of a interplanetary dust particle (IDP) on the surface of an atmosphereless body can create a huge amount of ejecta. The mass production rate is given by Krivov et al. (2003) and Spahn et al. (2006)

$$M^+ = F_{imp} Y S \tag{1}$$

the product of the IDP mass flux F_{imp}, the yield Y is the ratio of ejected mass to the projectile mass, and the cross section of target moon S. And the source rate is (Krivov et al., 2003; Spahn et al., 2006)

$$\dot{N}^+(>s) = \left(\frac{3-\gamma}{\gamma}\right)\left(\frac{M^+}{m_{\max}}\right)\left(\frac{s_{\max}}{s}\right)^{\gamma} \tag{2}$$

where $\gamma = 2.4$ is the power law index, s is the radius of particle, $s_{\max} = 100\,\mu\text{m}$ and $m_{\max} = 10^{-5}$ g are the maximum particle radius and mass, respectively.

The IDP mass flux F_{imp} at the Saturn environment is not yet well determined by observations, we adapt $F_{imp} = 9 \times 10^{-17}\,\text{g}\,\text{cm}^{-2}\,\text{s}^{-1}$ from Krivov et al. (2003), who used the Divine (1993) model. Note that the F_{imp} has considered the gravitational focusing of Saturn at distance of 3.2 R_s (Krivov et al., 2003; Spahn et al., 2006). The yield Y is also quite uncertain, it's value depends sensitively on surface properties which are poorly known. Nevertheless, we use the F_{imp} and follow Krivov et al. (2003) to obtain the values of Y by assuming a pure icy surface.

Both Methone and Anthe are so small that the initial ejecta speeds mostly exceed the escape speeds (v_{esc}) of the moons (0.49 m/s and 0.14 m/s). We assume the speeds of ejecta follow a distribution $n(v) \sim v^{-\beta}$ with $\beta = 2$ and $v_{esc} \leq v \leq 3$ m/s. Ejecta with initial speed $v > 3$ m/s are rare and are unlikely being confined in the arc. The resulting yields Y and source rates $\dot{N}^+$ are summarized in Table 1.

Table 1
The mean radii R of Methone and Anthe (Thomas et al., 2013), escape speed v_{esc}, the yield Y, and dust production rate $\dot{N}^+$ based on impact-ejecta model (Krivov et al., 2003; Spahn et al., 2006).

	R (km)	v_{esc} (m/s)	Y	$\dot{N}^+$ (s^{-1})
Methone	1.45	0.49	18,200	1.7×10^8
Anthe	0.5	0.14	17,900	2.0×10^7

2.2. Dust dynamics

The equation of motion for micron-sized particles in Saturn's E ring are given by

$$\begin{aligned} m\ddot{\mathbf{r}} = \quad & -m\nabla\Phi_S - \textstyle\sum_i GM_i m \frac{\mathbf{r}-\mathbf{r}_i}{|\mathbf{r}-\mathbf{r}_i|^3} \\ & +q[(\dot{\mathbf{r}} - (\Omega_s \times \mathbf{r})) \times \mathbf{B}] - \frac{I_\odot \sigma Q_{pr}}{c}\hat{e}_\odot + \mathbf{F}_D \end{aligned} \tag{3}$$

with the particle mass m and its acceleration $\ddot{\mathbf{r}}$. The vector $\mathbf{r}$ measures the location of the dust in an inertial frame originating in Saturn's center. On the right hand side, we have the gravity of oblate Saturn $\nabla\Phi_S$, where the gravitational potential Φ_S of an oblate body can be found in, for example, Murray and Dermott (2000). The second term is the gravity of the moons, where M_i and $\mathbf{r}_i$ are mass and position of the ith moon and G is the gravitational constant. Here we consider the gravity of the source moon (Methone or Anthe), Mimas, and Enceladus. Mimas introduces the resonances near Methone and Anthe orbits, and Enceladus is the massive moon outside the orbits of these smaller moons. The third term is the Lorentz force ($\mathbf{F}_L$), caused by the relative motion between the particle and Saturn's magnetic field. The charge of particles are denoted by q and the term $(\Omega_s \times \mathbf{r}) \times \mathbf{B}$ is corotational electric field, with spin rate of Saturn $\Omega_s = 1.6216 \times 10^{-4}$ rad/s (Gurnett et al., 2005) and Saturn's magnetic field $\mathbf{B}$, which is assumed to be a aligned dipole with the magnetic field strength at Saturn's equator −0.21 Gauss (Belenkaya et al., 2006). The charge is simply modeled by a constant surface potential of −4 V on a spherical dust grain, while observations by Cassini spacecraft suggests the surface potential of grains between Mimas and Enceladus orbit should be in the range of 0 V to −10 V (Sittler et al., 2006; Wahlund et al., 2005). The relation of surface potential ϕ and charge q is $\phi = (1/4\pi\epsilon_0)(q/s)$ where ϵ_0 is the vacuum permittivity and s the radius of particle. The solar radiation pressure ($\mathbf{F}_\odot$) is the fourth term, where $I_\odot \approx 14\,\text{W/m}^2$ is the solar energy flux at Saturn, c is the speed of light, Q_{pr} is the radiation pressure efficiency which is of order of unity, and is about 0.3 for icy particles with radius several micrometer or larger (Burns et al., 1979). Further, $\sigma = \pi s^2$ denotes the cross section of the particle and $\hat{e}_\odot$ is a unit vector pointing from the particle toward the Sun. The last term is the plasma drag $\mathbf{F}_D$ given by Eq. (12) later, which is dominated by the direct collisions between the particle and the bulk of plasma.

A more realistic model is to consider charging process (e.g., Horányi, 1996) and adopt a more accurate Saturn's magnetic field model (e.g., Burton et al., 2009). However, our simplification does not affect the result significantly because we are considering particles with radii larger than a few microns (for example, see Fig. 2). These 'larger' particles have small charge-to-mass ratios and the Lorentz force is less important than other perturbing forces. Thus they are not sensitive to the variations in charge or magnetic field. For this same reason, our result is not sensitive to minor changes in Saturn's spin rate Ω_s, whose value is yet uncertain (Helled et al., 2015; Lamy et al., 2011).

In the following, we briefly introduce the solar radiation pressure, plasma drag, and a confinement of the arcs by Mimas resonances.

2.2.1. Solar radiation pressure

Solar radiation pressure $\mathbf{F}_{\odot}$ leads to an increasing eccentricity, but due to the additional precession of the elliptical orbit due to Lorentz force and planetary oblateness the eccentricity performs a oscillation. A similar effect can be also observed in vertical direction for the inclination, although the passage of the particle through the planetary shadow is necessary. The forced components of orbital elements introduced by solar radiation pressure are given by Hedman et al. (2010a):

$$e = \frac{n}{\dot{\varpi}_0'}\left[3f(\epsilon)\frac{F_{\odot}}{F_S}\cos B_{\odot}\right]\sin(\dot{\varpi}_0 t/2) \tag{4}$$

$$\varpi - \lambda_{\odot} = \mathrm{mod}\left(\frac{\dot{\varpi}_0 t}{2}, \pi\right) + \frac{\pi}{2} \tag{5}$$

$$i = 2\frac{n}{\dot{\Omega}_0'}\left[g(\epsilon)\frac{F_{\odot}}{F_S}\sin|B_{\odot}|\right]\sin\left(\dot{\Omega}_0 t/2\right) \tag{6}$$

$$\Omega - \lambda_{\odot} = \mathrm{mod}\left(\frac{\dot{\Omega}_0 t}{2}, \pi\right) + \pi\frac{B_{\odot}}{|B_{\odot}|}\,. \tag{7}$$

where e is eccentricity, ϖ is longitude of pericenter, i is inclination, Ω is longitude of ascending node, n is the mean motion of particles, F_S is the gravity from Saturn, $B_{\odot}$ is the elevation angle of the Sun relative to ring plane (not to be confused with the Saturn's magnetic field $\mathbf{B}$ in Eq. (3)), and $\lambda_{\odot}$ is the longitude of the Sun. The precession rate of pericenter and precession rate of ascending nodes are $\dot{\varpi}_0' = \dot{\varpi}_0 - \dot{\lambda}_{\odot}$ and $\dot{\Omega}_0' = \dot{\Omega}_0 - \dot{\lambda}_{\odot}$, respectively, where $\dot{\varpi}_0 = \dot{\varpi}_{J2} + \dot{\varpi}_L$ and $\dot{\Omega}_0 = \dot{\Omega}_{J2} + \dot{\Omega}_L$ are precession rates introduced by the combination of planetary oblateness ($\dot{\varpi}_{J2}$ and $\dot{\Omega}_{J2}$) and Lorentz force ($\dot{\varpi}_L$ and $\dot{\Omega}_L$), $\dot{\lambda}_{\odot}$ is the slow seasonal variation of the solar longitude. The precession rates induced by planetary oblateness and Lorentz force have been modeled by Horányi et al. (1992), this gives $\dot{\varpi}_{J2} \approx |\dot{\Omega}_{J2}| \approx 0.85$ deg/day (by using the gravitational harmonic coefficient $J_2 = 0.01629071$, Jacobson et al., 2006) near Methone's orbit and 0.8 deg/day near Anthe's orbit, while by Lorentz force $\dot{\varpi}_L = -0.66(\phi/-4V)(1\,\mu\mathrm{m/s})^2$ deg/day near Methone's orbit and $\dot{\varpi}_L = -0.63(\phi/-4V)(1\,\mu\mathrm{m/s})^2$ deg/day near Anthe's orbit. In practice, $\dot{\lambda}_{\odot}$ is very small ($\sim$12 deg/yr $\approx$ 0.03 deg/day) in comparison to the precession rates dominated by planetary oblateness or Lorentz force and thus will be ignored for the current problem. The definitions $f(\epsilon) = 1 - \epsilon + \sin(2\pi\epsilon)/6\pi$, and $g(\epsilon) = \sin(\pi\epsilon)/\pi$ are used in Hedman et al. (2010a) obtained by the averaging over one particle orbit, where ϵ is the fraction passage time of the shadow during one particle orbit.

By applying the model above, particles near Methone achieve a forced eccentricity and inclination of

$$e_f \approx 4.69 \times 10^{-2} f(\epsilon)\cos B_{\odot}\frac{Q_{pr}}{s/1\,\mu\mathrm{m}} \tag{8}$$

$$i_f \approx 3.13 \times 10^{-2} g(\epsilon)\sin|B_{\odot}|\frac{Q_{pr}}{s/1\,\mu\mathrm{m}}, \tag{9}$$

and slightly different at Anthe orbit

$$e_f \approx 4.38 \times 10^{-2} f(\epsilon)\cos B_{\odot}\frac{Q_{pr}}{s/1\,\mu\mathrm{m}} \tag{10}$$

$$i_f \approx 2.93 \times 10^{-2} g(\epsilon)\sin|B_{\odot}|\frac{Q_{pr}}{s/1\,\mu\mathrm{m}} \tag{11}$$

where $\epsilon \leq 0.10$ at Methone and Anthe orbit, $B_{\odot}$ varies between $\pm 26.7°$, and $Q_{pr} \approx 0.3$ for particles larger than a few microns, as mentioned earlier. Note that ϵ is also a function of $B_{\odot}$, and ϵ can be zero while the Sun is high above the ring plane. For particles near Methone and Anthe orbits $f(\epsilon)\cos(B_{\odot})$ ranges from 0.89 to 0.93, whereas $g(\epsilon)\sin(|B_{\odot}|)$ spans values between 0 and 0.044.

2.2.2. Plasma drag

To estimate the strength of plasma drag one first needs to know the plasma ion densities. The sources of plasma in the innermost region of the E ring (3–4 R_s) are Enceladus and the ionization of the main ring O_2 atmosphere (Elrod et al., 2012; 2014; Johnson et al., 2006; Tseng et al., 2010). In this region, observations by Cassini spacecraft show that the heavy ion densities (water group ions and O_2^+) are about 1–100 cm^{-3}, and are highest near the Enceladus orbit (Elrod et al., 2014). Furthermore, there are seasonal variations of the ion densities, i.e., the ion densities are higher while the Sun is high above ring plane (Elrod et al., 2012; 2014; Tseng et al., 2010). To simplify the problem, we assume there are O^+ ions with constant densities of 43.2 cm^{-3} in Methone's orbit and 44.0 cm^{-3} in Anthe's orbit. These values are obtained by a simple assumption that the number densities of these ions are increased linearly from 40 cm^{-3} at orbit of Mimas ($\sim$3.08 R_s) to a peak value at orbit of Enceladus ($\sim$3.95 R_s) with density 53 cm^{-3} (Münch, 2013).

The force due to plasma direct collision is given by Banaszkiewicz et al. (1994)

$$F_D = \pi n_i m_i u_i^2 s^2\left[\left(M_i + \frac{1}{2M_i}\right)\frac{\exp(-M_i^2)}{\sqrt{\pi}} + \left(M_i^2 + 1 - \frac{1}{4M_i^2}\right)erf(M_i)\right]. \tag{12}$$

The ions are characterized by their number density n_i, thermal velocity u_i, and mass m_i, respectively. The Mach number is defined by $M_i = \tilde{v}_0/u_i$, where $\tilde{v}_0$ is the velocity of a particle relative to bulk plasma. The Mach number relative to O^+ ions in Methone and Anthe orbit are both about 1.2.

Plasma can also interact with charged particles via Coulomb forces (Northrop and Birmingham, 1990). This indirect 'Coulomb drag' is ignored in our model, because at 3–4 R_s the Coulomb drag is much weaker than the contribution via plasma direct collisions $\mathbf{F}_D$. In the Saturn environment, Coulomb drag is important when the Mach number is about unity, e.g., in the A ring, including the Encke gap (Grün et al., 1984; Sun et al., 2015).

In the inner part of the E ring, plasma nearly corotates with Saturn. The corotation speed is faster than the Keplerian speed of particles outside the synchronous radius of 1.86 R_s. Collisions with ions push particles roughly in direction of the orbital motion, this means particles gain orbital energy and angular momentum and therefore they are migrating outward. By utilizing the Gaussian perturbation equations (e.g., Burns, 1976), the plasma drag induces an increase of semi-major axes near Methone and Anthe in the rate

$$\frac{da}{dt} \approx 600\left(\frac{1\,\mu\mathrm{m}}{s}\right)\mathrm{km\,yr^{-1}}. \tag{13}$$

In other words, 1 μm particles can migrate outward by about 0.3 R_s in one Saturnian year.

2.2.3. Mimas resonances and perturbing forces

Particles ejected from the surface of Methone and Anthe are likely trapped in the same resonances as their source moons (Fig. 1, also see Cooper et al., 2008 and Hedman et al., 2009). However, perturbing forces complicate the situation, especially the drag force that pushes the particles outward. Roughly speaking, the probability of trapping migrating particles is higher if the migration rate is lower (e.g., Dermott et al., 1994; Wyatt, 2003; Vitense et al., 2012; Shannon et al., 2015). In this case, the migration rate da/dt is induced by plasma drag and the value is inverse proportional to particle size (Eq. (13)), this means large particles migrate slower and therefore are more likely to be trapped in the resonances.

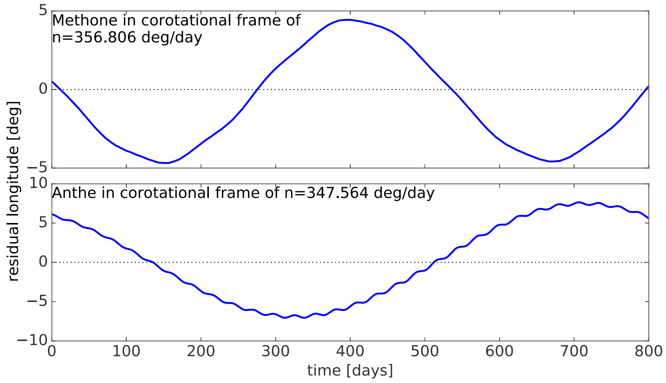

Fig. 1. Simulation result of the residual longitudes of Methone and Anthe in the corresponding corotational frames. The software for the simulation is described in Section 3.1. The starting date of the simulation is May 30, 2007 (date of discovery of Anthe, Porco, 2007). The initial position and velocity of moons (Mimas, Methone, Anthe, Enceladus) are adapted from JPL's HORIZON system. As shown in figure, the libration period is roughly 520 days for Methone, and 800 days for Anthe.

2.3. Sinks

Particles ejected from Methone and Anthe may get caught in the arcs or escape and continuously migrate outward due to plasma drag. For particles in the arcs, the dominating particle sinks are the parent moons embedded in the arcs. Particles escaping the arcs migrate outward until they reach Enceladus' orbit, where they collide with Enceladus or drift beyond it's orbit. The lifetimes of particles are in the order of 100 years, as shown later in Fig. 10.

The erosion of particles by plasma sputtering requires longer timescales (Johnson et al., 2008), but at least it sets an upper limit on particles' lifetime. The plasma sputtering rate in the inner E ring is on the order of 1 μm radius every 100 years (Johnson et al., 2008). We use a slightly smaller value (0.6 μm per 100 years) because the sputtering rate at Methone's and Anthe's orbits is slightly smaller due to the lower plasma density (see Fig. 3 in Johnson et al., 2008). With this value, the sputtering lifetime is

$$T_{sput} = 167\left(\frac{s}{1\,\mu\mathrm{m}}\right)\ \text{years} \tag{14}$$

where s is the particle radius. Practically, particles never reach such long lifetimes. As shown later in Fig. 10, small particles are unstable in the arcs due to perturbing forces and therefore almost are not confined in the arcs, while larger ones (10–40 μm) usually stay in the arc for more than 100 years. For larger particles, 100 years means their radii only decrease by about 1 μm, and therefore their dynamics do not change significantly. This implies our result is not sensitive to erosion rate.

3. Numerical simulations

3.1. Configuration of simulation

In order to find the distribution of dust near Methone and Anthe, the equations of motion Eq. (3) have been numerically integrated using the RADAU integrator (Everhart, 1985) implemented in the MERCURY package (Chambers, 1999). In addition to the perturbing forces, the plasma sputtering rate of 0.6 μm per 100 year is considered, i.e., particle radii are decreasing with time. The initial conditions of the massive moons (Methone, Anthe, Mimas, Enceladus) are adapted from JPL's HORIZON system. The simulation stops once all test particles are removed – either by collision with Methone, Anthe, Mimas, Enceladus, or when their radial position is inside Mimas' orbit or outside Enceladus' orbit.

Particles are ejected randomly from the surface of Methone and Anthe with speed distribution $n(v) \sim v^{-2}$ in the range $v_{esc} \le v \le 3\,\mathrm{m/s}$ (as described in Section 2.1), constant elevation angle of 45° relative to the surface of moon and randomly chosen azimuthal angles. The radius of the ejecta s is also assumed to obey a power law distribution $n(s) \sim s^{-\gamma}$, with $\gamma = 2.4$ and $1 \le s \le 40\,\mu$m, also mentioned in Section 2.1.

Note that instead of using maximal particle size of 100 µm as mentioned earlier in Section 2.1, we use $s_{\max} = 40\,\mu\mathrm{m}$ in the simulation for simplicity. This should not change the result significantly. These larger particles have longer lifetimes and therefore contribute to the brightness of the arcs. It is shown in Fig. 2 that the particle size distributions in the steady-state arcs are flatter than -2.4 (the ejecta size distribution), implying the lifetimes are correlated to particle size. More detail about lifetimes and particle size is discussed later in Fig. 10 and Section 3.3. But on the other hand: (1) larger particles are rare according to the power law distribution; (2) since the mass production rate M^+ is constant for same impactor and same targets, including these larger particles mean there are less smaller ones (e.g., the dashed lines in Fig. 2 should be lower), which may compensate the contribution from these larger particles. Therefore including larger particles in the simulation should not change the result significantly.

We choose the particle radii randomly between 1 and 40 μm in the simulation and weight the resulting density with the according power law distribution. The benefit of weighting later is that one does not need to run simulations with a lot of tiny particles and only a few large particles, i.e., there is no need to simulate huge amount of particles to reach reasonable numerical result. Similar procedures have been applied to the Phoebe ring (Hamilton et al., 2015) in the comparison of the size distribution to the observed data.

As shown in Fig. 1, Methone and Anthe are both librating around a stable corotational point for the Mimas resonance. This

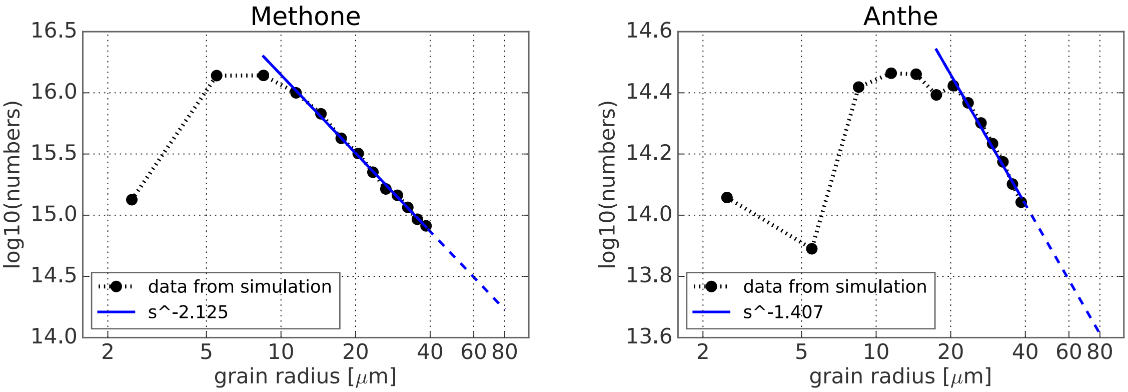

Fig. 2. Simulation result of the size distribution in the steady-state arcs.

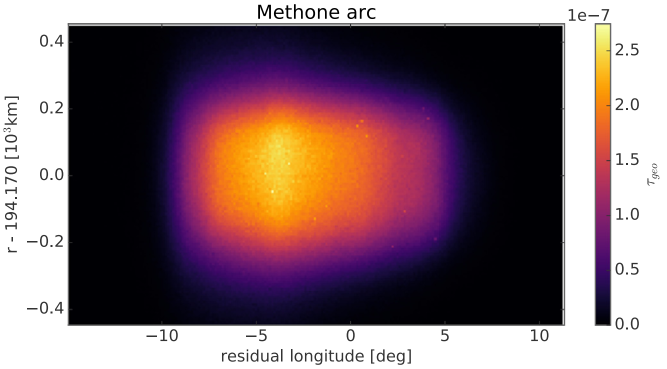

Fig. 3. Simulation results giving the geometric optical depth of Methone arc in the longitudes and radial distance relative to mean motion of 356.806°/day, which correspond to $a = 194{,}173.832$ km.

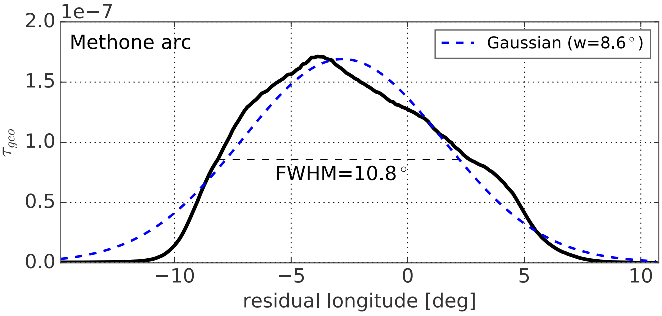

Fig. 4. Longitudinal scan of Methone arc. The geometric optical depth is average over radial distance between 193,741 and 194,568 km. The dashed line is the best fit of Gaussian with width ≈ 8.6°, while FWHM ≈ 10.8° in our result.

is also considered in simulation. Particles are ejected from surface of Methone or Anthe at 14 different phases of each libration.

We use the following procedure to map the simulation data to the real numbers, which is similar to the methods used by Juhász and Horányi (2002). After weighting to the power law size distribution, the total number of particles in the beginning of simulation is N_{sim0}, this number should be scaled to number of dust produced per unit time $\dot{N}^+$, as summarized in Table 1. In each simulation, we only eject particle at one single time and have particle orbits stored in equal time steps Δt. To map the simulation data to real numbers, we count the cumulative number of particles in a 'box' N_{sim}, the box can be a grid in $x-y$ plane or in longitude-radius grids. After all these calculations, the real number of particles in the box is

$$N = N_{sim}\frac{\dot{N}^+}{N_{sim0}}\Delta t. \qquad (15)$$

3.2. Methone and Anthe arcs

We have simulated the entire 'life' of about 4000 test particles starting at both Methone and Anthe. Figs. 3 and 6 show the geometric optical depth in the corotating frame of Methone and Anthe. For both arcs we choose corotating frames with mean motions of 356.806 deg/day for the Methone arc and 347.564 deg/day for the Anthe arc, which are the same values we used in Fig. 1. These mean motions correspond to the averaged mean motion of Methone or Anthe in the whole simulation period ($>$ 100 years). Geometric optical depth is the optical depth without considering any light scattering or extinction by particles, in other words, assuming the extinction efficiency $Q_{ext} = 1$. Therefore the geometric optical depth is simply the fraction of the total cross section of ring particles in an area. Note that in the following we only consider the geometric optical depth in the direction normal to ring plane. As shown in Figs. 4 and 7, the full width at half maximum (FWHM) of Methone and Anthe arcs are 10.8° and 15.0°, while observations by Hedman et al. (2009) yielded longitudinal extension about 10° and 20°, respectively.

Figs. 5 and 8 show the radial and longitudinal profiles of both arcs. These are the average profiles of simulation result, with the number of particles counted by Eq. (15). The average radial profiles of the arcs are presented in the left panels of Figs. 5 and 8. The FWHM of both radial profiles are around 500 km, this corresponds to eccentricities of about 0.0013. The eccentricity of Methone/Anthe is about 0.0015/0.001, which could explain the eccentricities of arc materials. How about the forced eccentricities induced by solar radiation pressure? Based on Eqs. (8) and (10), the forced eccentricities for particles in Methone/Anthe arcs are $0.013/(s/1\,\mu\mathrm{m})$ and $0.012/(s/1\,\mu\mathrm{m})$, respectively. Since both arcs are dominated by grains with radii between 5–10 μm (as shown in Fig. 2), the forced eccentricities induced by solar radiation pressure are close to the eccentricities of the source moons.

The average vertical distributions of the arcs are shown in the right panels of Figs. 5 and 8. Just like the eccentricities, the inclinations are mainly the inclinations of the source moons. The inclinations of Methone and Anthe are 0.025° and 0.02°, implying

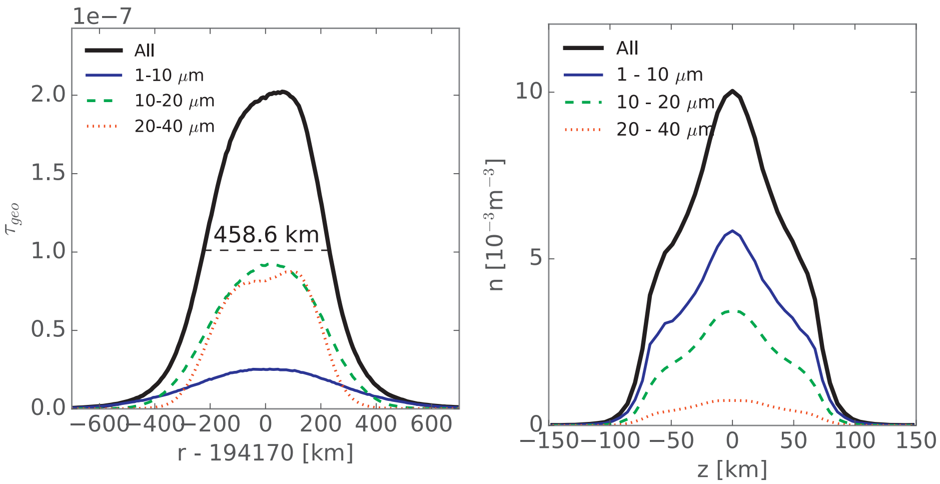

Fig. 5. Radial and vertical distribution of particles in Methone arc. The radial profile is averaged over the FWHM of residual longitudes, the dashed line is the FWHM of the radial profile. The vertical profile is averaged over the center of arc – the FWHM of both residual longitudes and radial distances.

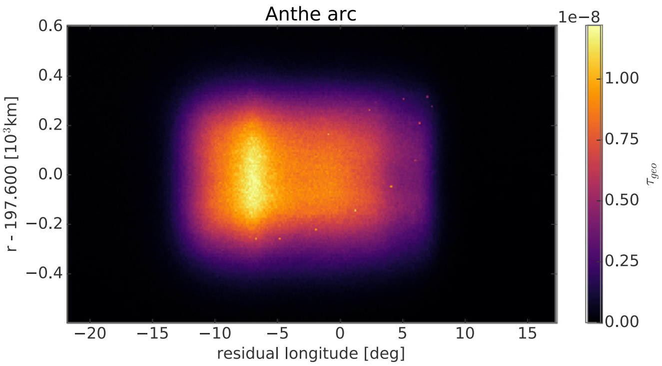

Fig. 6. Simulation results giving the geometric optical depth graph of Anthe arc in the longitudes and radial distance relative to mean motion of 347.564°/day, which correspond to a = 197,595.413 km.

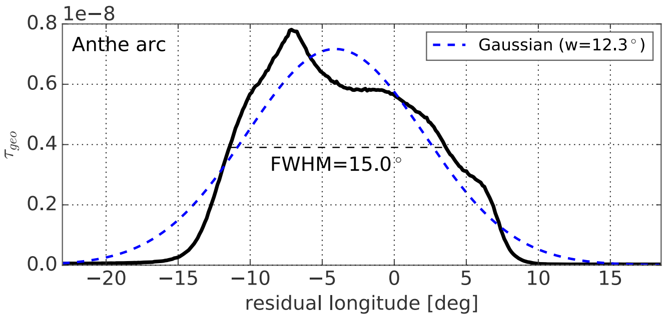

Fig. 7. Longitudinal scan of Anthe arc. The geometric optical depth is average over radial distance between 197,194 to 198,021 km. The dashed line is the best fit of Gaussian with width ≈ 12.3°, while FWHM ≈ 15° in our result.

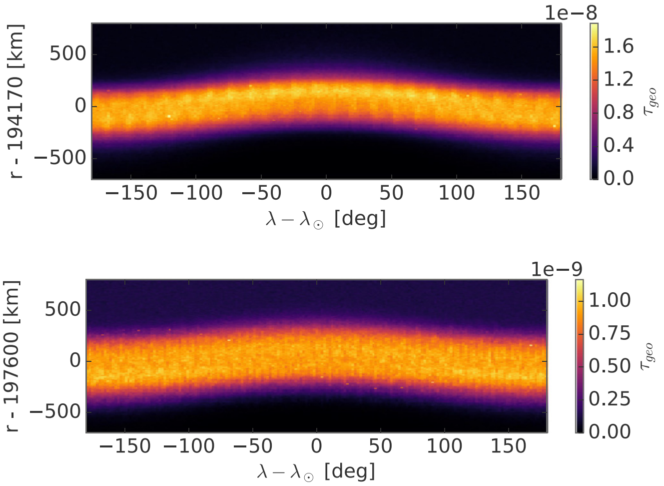

Fig. 9. Heliotropic Methone (upper) and Anthe (lower) arc materials, accumulated over time and therefore spanning over all longitudes relative to the Sun. $\lambda_\odot$ is longitude of the Sun and λ is longitude of particle.

vertical displacements ($a \times i$) of 84 km and 69 km, respectively. On the other hand, the maximal forced inclinations introduced by solar radiation pressure (Eqs. (9) and (11)) are about $(0.024/(s/1\,\mu\text{m}))^\circ$, or $ai \approx 82/(s/1\,\mu\text{m})$ km. Our results show a double peak feature in the vertical profile of the Anthe arc, but not in the Methone arc. The double peak feature in vertical profile implies the narrow distribution of inclinations, which is also seen in the ejecta from Enceladus (Juhász et al., 2007; Kempf et al., 2008; Kurth et al., 2006), the gossamer ring of Jupiter (Burns et al., 1999), and the Phoebe ring (Verbiscer et al., 2009). In our simulation, Methone's inclination ranges between 0.006° and 0.020°, while Anthe's inclination ranges between 0.012° and 0.020°. The amplitude of Anthe's inclination is smaller, thus the inclinations of Anthe's ejecta are also more concentrated. This could explain the double peak feature in vertical profile of the Anthe arc but not in the Methone arc.

Either in the arc or not, micron-sized grains are in heliotropic orbits, as shown in the simulation result in Fig. 9. The *average* pericenter of ring particles is oriented in the anti-solar direction, same as predicted in Eq. (5).

It is expected that larger particles can stay in the arc for longer time due to their smaller migration rate da/dt. We crudely estimate the time particles stay in arc by checking the time they reach certain semi-major axes. Simulations show that the libration amplitudes in semi-major axes for particles in the arcs are about < 40 km, and we assume particles with semi-major axes more than 100 km from their moons' average semi-major axis have left the arcs. This position is not quite accurate but sufficient to measure the lifetimes inside the arc. The result is presented in Fig. 10, which shows trends of particle radii and maximal time particle stay in arcs. Fig. 10 also shows that there is a critical radius of ~5 μm for Methone arc and ~10 μm for Anthe arc, grains smaller than these critical radii can only stay in arc for a few years, while larger ones can stay for more than 100 years. The particles smaller than the critical radius are never confined in the

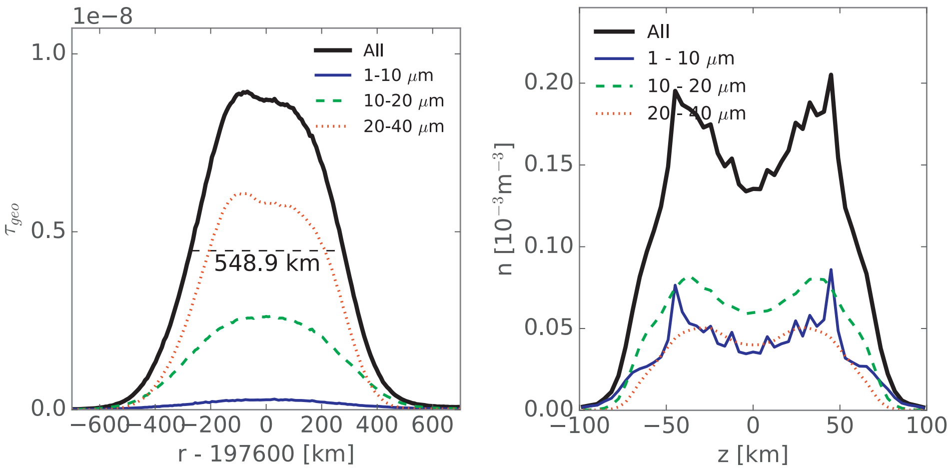

Fig. 8. Radial and vertical distribution of particles in Anthe arc. The radial profile is averaged over the FWHM of residual longitudes, the dashed line is the FWHM of the radial profile. The vertical profile is averaged over the center of the arc – the FWHM of both residual longitude and radial distances.

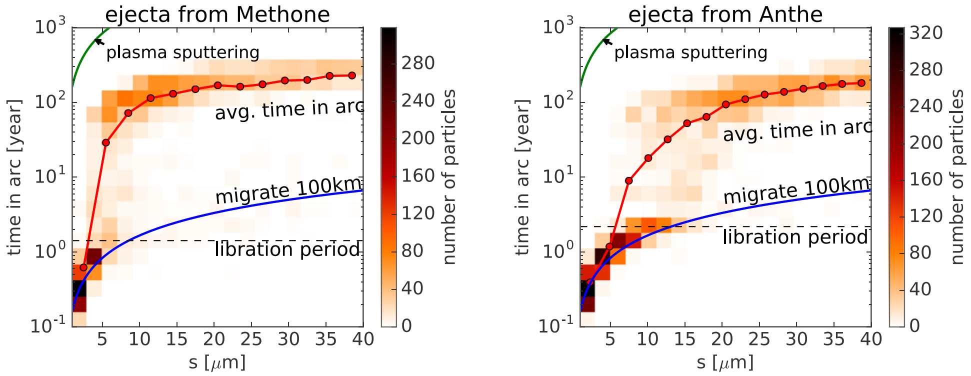

Fig. 10. The relationship of initial particle radii and time spend or confined in the arc. Particles collide with source moons are not counted here. The green curve on top left is the sputtering lifetime T_{sput} described in Eq. (14). The libration period is the time for the source moons to finish one libration around the stable co-rotation point, which is about 520 days for Methone and 800 days for Anthe. The blue lines plot the time required for grain of radius s to migrate outward by 100 km of semi-major axes by plasma drag. (For interpretation of the references to color in this figure legend, the reader is referred to the web version of this article.)

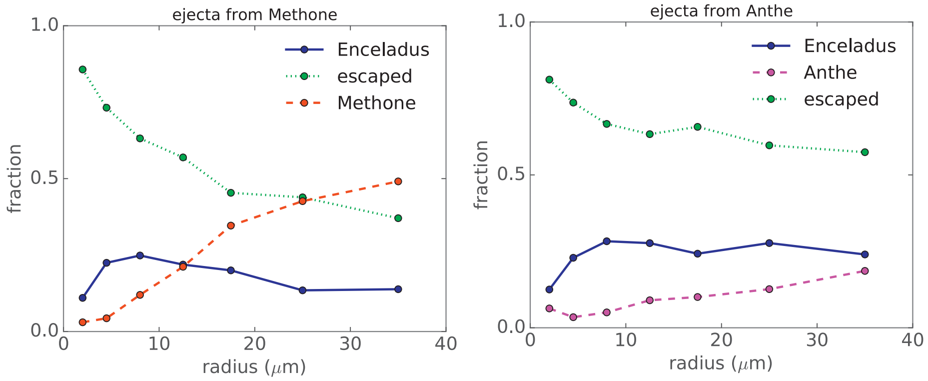

Fig. 11. Percentage of sinks of particles by particle initial radius. There are less than 1% of Methone ejecta collide with Mimas and is ignored in this plot.

Table 2
Sinks of ejecta in simulation, compare with the total ejected number of particles. 'Escaped' particles are removed from simulation once their radial distance is outside Enceladus orbit or inside Mimas orbit. Note there is also 0.22% of ejecta from Methone collide with Mimas due to their large eccentricities.

Source moon	Sinks (%)			
	Methone	Anthe	Enceladus	escaped
Methone	3.94	–	13.00	82.84
Anthe	–	6.02	14.50	79.48

corresponding resonances. This explains the particle size distribution in the steady-state arcs shown in Fig. 2.

In our simulations, the main reason for particles to leave the arcs is plasma drag, while other perturbing forces may also have minor effects in determining the lifetime. Gravitational scattering by Methone or Anthe is not found in simulations, which is expected since their Hill spheres are just a bit larger than their radii. The radii of Hill spheres are 2.8/0.9 km for Methone/Anthe. Plasma sputtering have in principle no impact on particle lifetimes, as shown in the green lines in Fig. 10.

3.3. Sinks of ejecta

The percentage of particle numbers for each sinks is summarized in Table 2. For ejecta from Methone, $\sim$4% recollide to Methone, $\sim$13% collide with Enceladus, and $\sim$83% reach orbits further outside. The fate of ejecta from Anthe ejecta are similar: $\sim$6% recollide to Anthe, $\sim$15% collide with Enceladus, and $\sim$79% escaped the region of interest. Escaped particles reach orbits outside the radial position of Enceladus due to plasma drag, except a few particles with pericenter inside the orbit of Mimas due to their high eccentricities. Only 0.22% of the ejecta from Methone collide with Mimas.

Due to the difference in their dynamics, large and small particles have quite different fates, as shown in Fig. 11. Larger particles are more likely to collide with the source moons because in average they are confined in the arcs for longer time. The smaller cross section of Anthe may explain why fewer large particles recolliding with Anthe in comparison to the amount of large particles recolliding with Methone.

4. Discussion

4.1. Simulation vs. observation

Our results show that the geometric optical depths in the order of 10^{-8}–10^{-7}, or number densities of 10^{-4}–10^{-3} m^{-3}. In Fig. 12 we compare the radial profiles of Anthe arc with observed brightness (normal I/F). These observational profiles are the average of three subsequently images taken within an hour while the solar longitudes are between 66° and 75° and phase angle $\sim$23°, and these images are processed by the methods described in Hedman et al. (2009). During the time of observation, Anthe should be located at residual longitude (λ_{resi}) close to $-8°$ (see Fig. 9 in Hedman et al., 2009).

As shown in Fig. 12, the optical depths obtained from our simulation have to be multiplied by a factor of $\sim$14 so that the peak value is same as in the observational brightness. Since our simulation result contains mainly particles larger than $5\,\mu$m and the phase angle in the observation is only $\sim$23°, the brightness can be

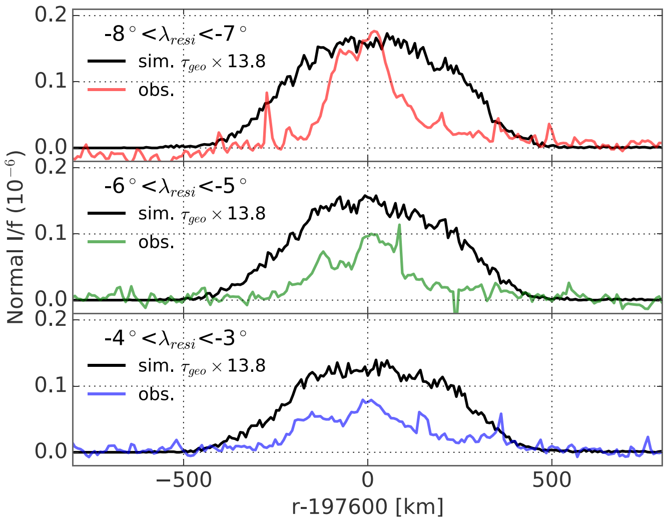

Fig. 12. Radial profiles of observation and simulation results of Anthe arc along different residual longitudes (λ_{resi}). The observational data are obtained from the average of three subsequently images (file names: N1586002250, N1586003083, N1586004500) with solar longitudes between 66° and 75° and phase angle ~23°. The red, green, and blue curves are the radial profiles at different longitudes. Some of the spikes in observational data are from background stars, such as the peaks close to −300 km in red curve, near 100 km in green curve, and near 150 and 350 km in blue curve. (For interpretation of the references to color in this figure legend, the reader is referred to the web version of this article.)

approximated as the optical depths times the albedo of the particles. The albedo of the arc material should be close to one, similar to icy moons in the Saturn E ring (Verbiscer et al., 2007). This means the simulated results are about 14–20 times (for albedo between 0.7 and 1) smaller than the observed value. Plausible explanations for the difference include the uncertainties of $F_{imp}\times Y$ and additional sources of dust. As mentioned earlier in Section 2.1, both values of impactor flux F_{imp} and yields Y are highly uncertain and could leads to order(s) of magnitude different from our estimated values. In the following we discuss the possibility of additional dust sources.

There may exist a belt of millimeter-radius particles, which can act as additional dust sources. The absorption of electrons observed by Cassini Low Energy Magnetospheric Measurement System (LEMMS) near Methone's orbit can be explained by an arc composed of particles larger than a millimeter near Methone, and their optical depth is below the detection limit (Roussos et al., 2008). These 'large' particles could also be the source of smaller ones via impact-ejecta process. Assuming the optical depth of these larger particles is 10^{-6}, and they fill the 24° Methone arc center at radial distance of Methone (194, 170 km) with radial width of 100 km, then the total cross section of large particles is about 8.1 km^2. This is slightly larger than the cross section of Methone (~6.6 km^2). Since the dust production rate is proportional to the cross section (Eq. (1)) as long as all ejecta can escape their source, this implies the source rate (and therefore the brightness) can be doubled. Unfortunately, it is difficult to have further detections or hints on the existence and population of these mm-sized particles. It is essential to have further theories and observations to constrain F_{imp}, Y, and mm-sized particles as the additional source.

In addition to interplanetary dust particles (IDPs), E ring particles (ERPs) also impact on these tiny moons and eject dust. Spahn et al. (2006) estimated that ERPs could produce dust as efficient as IDPs for the moons in the inner E ring (see summary for in Table 2 for Mimas there): the ERP impactor flux is about 3–4 orders larger than IDP, and the ERP impactor speed could reach several km/s (assuming eccentricity of ERPs reach 0.5), which is similar to IDP. Although ERPs are typically much smaller than IDPs (about 1 μm compare with 100 μm), but ERP flux is much larger than IDP flux, therefore the ERP flux could be as important as IDP flux in producing dust through impact-ejecta process for these inner E ring moons.

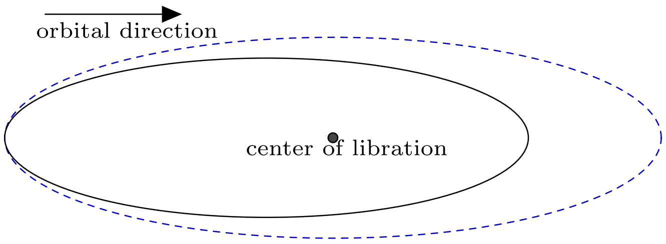

Fig. 13. This cartoon illustrates how drag force cause the longitudinal asymmetry of arc, as seen in Figs. 3 and 6. Arc material are librating around center of libration. Without drag, particles librate inside the dashed curve, can form longitudinal distribution similar to the dashed line in Figs. 14; with drag, particles librate inside the asymmetric ellipse.

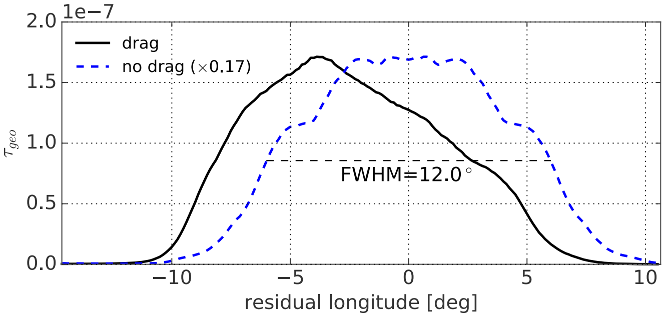

Fig. 14. Longitudinal scan of Methone arc with drag force (solid line, same as Fig. 4) and the simulation without drag force (dashed line). The geometric optical depth of the no-drag case has been scaled to the same level as the former.

4.2. Longitudinal asymmetric arc

In the limited amount of observations by Cassini ISS, Anthe is found in the back (relative to orbital direction) and middle of the arc, this can be explained by the moon and arc material are both librating around a stable co-rotation point of the Mimas resonance at different phases (Hedman et al., 2009). Additionally, our simulation results show that the averaged relative longitudes of arc materials are behind Methone's and Anthe's mean position by about 4° and 7°, as shown in Figs. 3 and 6.

This longitudinal asymmetry could be explained by combination of resonance trapping and drag force. As illustrated in Fig. 13, in the corotational frame of center of libration, particles librate inside the dashed curve while there is no drag force. With drag force, particles librate and also migrate outward, therefore the orbital velocities (around Saturn) are decreasing. While the orbital velocities are smaller than that of the center of libration, they start to move backward in this corotational frame (toward left of Fig. 13). This means these particles cannot reach the leading longitudes and only librate inside a smaller region, such as the solid curve in Fig. 13. To verify this, we run a set of simulations of ejecta from Methone without plasma drag in order to compare with our simulation where drag force has been considered. The result is in Fig. 14. As expected, it shows a symmetric distribution of particle longitudes. The same idea of the combination of drag force and resonance has been used to explain the longitudinal asymmetry of a ringlet in the Encke gap of Saturn's A ring (Hedman et al., 2013; Sun et al., 2015).

Unfortunately, such longitudinal shifts are difficult to confirm with the limited amount of observations currently available. If there are chances to quantify the longitudinal shift, one can obtain information about the strength of plasma drag, which is sensitive to the ion densities and particle size distribution. For example, smaller particles experienced larger drag force and thus should be confined in a smaller region, thus they should span only a few degrees longitudinally centered at the peaks in Figs. 4 and 7.

5. Summary and future work

We use numerical simulations to estimate the distribution and amount of dust in Methone's and Anthe's arcs. To do this, we model the source, the dynamical evolution, and the sinks of particles. We use the impact-ejecta model (Krivov et al., 2003; Spahn et al., 2006) to estimate the source rate of particles. For the dynamical evolution, we consider these perturbing forces: oblateness of Saturn, solar radiation pressure, Lorentz force, and plasma drag. Mimas and Enceladus are both considered in simulation: Mimas plays an important role in confining the arc material, while Enceladus is the massive moon outside the orbit of these two arcs. The dominant mechanism responsible for removing particles from the arc is plasma drag which increases the particles' orbital energy. About 10–20% of all ejecta end on Enceladus. If we only consider the larger particles ($s > 10\,\mu$m), recollision with the source moons is as important as migrating outward. The lifetimes of arc particles, defined by the time particles stay at semi-major axes close to the source moons, are also related to particle size. Smaller ones do not stay in arc and leave the arcs at a rate of outward migration driven by plasma drag. Grains with radii larger than $5\,\mu$m can stay in arc on a timescale of 100 years. The erosion of particles by plasma sputtering is also taken into account, but has almost no impact since it sets a maximal lifetime of particles that is much larger than other sinks.

Our results show that the longitudinal extension of the Methone/Anthe arc is 10.8°/15°, which are consistent with observations and theory. Simulation results also show that the optical depths of both arcs are in the order of 10^{-8}–10^{-7}, or number densities in the order of 10^{-4}–$10^{-3}\,\mathrm{m}^{-3}$. Comparing our Anthe arc simulation result with observation, our peak brightness is about 14–20 times smaller (Fig. 12). Plausible explanations of the brightness difference include the highly uncertain impactor flux F_{imp} and yields Y, and mm-sized particles as additional dust sources. It is essential to have further theories and observations to constrain these parameters and speculations further.

This model could be applied to other diffuse rings with embedded moon(s). For example, Pallene is another tiny moon (radius ~2.2 km, Thomas et al., 2013) between Mimas and Enceladus orbit. Observations show that there is a torus near the orbit of Pallene (Hedman et al., 2009; Seiß et al., 2014), with radial and vertical FWHM of 2, 300 km and 270 km, respectively (Seiß et al., 2014). Just like the Methone and Anthe arcs, the impact-ejecta process is proposed to be the dust source of the torus (Hedman et al., 2009; Seiß et al., 2014). Unlike Methone or Anthe, Pallene is not in first order resonance (Hedman et al., 2009). Ejecta from Pallene are therefore not confined in the semi-major axis close to Pallene but are migrating outward due to plasma drag. Further studies are required to understand whether Pallene itself is sufficient as the dust source, or other sources or confinement of dust (such as higher order resonances) are required.

Acknowledgments

We thank Mihály Horányi and an anonymous reviewer for the constructive reports. The work is supported by DFG SP 384/21-1 and DLR 50OH1401.

References

Banaszkiewicz, M., Fahr, H.J., Scherer, K., 1994. Evolution of dust particle orbits under the influence of solar wind outflow asymmetries and the formation of the zodiacal dust cloud. Icarus 107 (2), 358–374.

Belenkaya, E.S., Alexeev, I.I., Kalegaev, V.V., Blokhina, M.S., 2006. Definition of Saturn's magnetospheric model parameters for the Pioneer 11 flyby. Ann. Geophys. 24 (3), 1145–1156.

Burns, J.A., 1976. Elementary derivation of the perturbation equations of celestial mechanics. Am. J. Phys. 44 (10), 944.

Burns, J.A., Lamy, P.L., Soter, S., 1979. Radiation forces on small particles in the solar system. Icarus 40 (1), 1–48.

Burns, J.A., Showalter, M.R., Hamilton, D.P., Nicholson, P.D., de Pater, I., Ockert-Bell, M.E., Thomas, P.C., 1999. The Formation of Jupiter's Faint Rings. Science 284, 1146–1150.

Burton, M.E., Dougherty, M.K., Russell, C.T., 2009. Model of Saturn's internal planetary magnetic field based on Cassini observations. Planet. Space Sci. 57 (1), 1706–1713.

Chambers, J.E., 1999. A hybrid symplectic integrator that permits close encounters between massive bodies. Mon. Not. R. Astron. Soc. 304 (4), 793–799.

Cooper, N.J., Murray, C.D., Evans, M.W., Beurle, K., Jacobson, R.A., Porco, C.C., 2008. Astrometry and dynamics of Anthe (S/2007 S 4), a new satellite of Saturn. Icarus 195 (2), 765–777.

Dermott, S.F., Jayaraman, S., Xu, Y.L., Gustafson, B.Å.S., Liou, J.C., 1994. A circumsolar ring of asteroidal dust in resonant lock with the Earth. Nature 369 (6483), 719–723.

Dikarev, V.V., 1999. Dynamics of particles in Saturn's E ring: effects of charge variations and the plasma drag force. Astron. Astrophys. 346, 1011–1019.

Divine, N., 1993. Five populations of interplanetary meteoroids. J. Geophys. Res. 98 (E), 17029–17048.

El Moutamid, M., Sicardy, B., Renner, S., 2014. Coupling between corotation and Lindblad resonances in the presence of secular precession rates. Celestial Mech. Dyn. Astron. 118 (3), 235–252.

Elrod, M.K., Tseng, W.L., Wilson, R.J., Johnson, R.E., 2012. Seasonal variations in Saturn's plasma between the main rings and Enceladus. J. Geophys. Res. 117 (A3), A03207.

Elrod, M.K., Tseng, W.L., Woodson, A.K., Johnson, R.E., 2014. Seasonal and radial trends in Saturn's thermal plasma between the main rings and Enceladus. Icarus 242, 130–137.

Everhart, E., 1985. An efficient integrator that uses Gauss-Radau spacings. Dyn. Comets 1, 185.

Grün, E., Morfill, G. E., Mendis, D. A., 1984. Dust-magnetosphere interactions. IN: Planetary rings (A85-34401 15-88). Tucson, 275–332.

Gurnett, D.A., Kurth, W.S., Hospodarsky, G.B., Persoon, A.M., Averkamp, T.F., Cecconi, B., Lecacheux, A., Zarka, P., Canu, P., Cornilleau-Wehrlin, N., Galopeau, P., Roux, A., Harvey, C., Louarn, P., Bostrom, R., Gustafsson, G., Wahlund, J.E., Desch, M.D., Farrell, W.M., Kaiser, M.L., Goetz, K., Kellogg, P.J., Fischer, G., Ladreiter, H.P., Rucker, H., Alleyne, H., Pedersen, A., 2005. Radio and plasma wave observations at Saturn from Cassini's approach and first orbit. Science 307 (5713), 1255–1259.

Hamilton, D.P., Skrutskie, M.F., Verbiscer, A.J., Masci, F.J., 2015. Small particles dominate Saturn's Phoebe ring to surprisingly large distances. Nature 522 (7555), 185–187.

Hamilton, D.P., 1993. Motion of dust in a planetary magnetosphere-Orbit-averaged equations for oblateness, electromagnetic, and radiation forces with application to Saturn's E ring. Icarus 101, 244–264.

Hedman, M.M., Burns, J.A., Hamilton, D.P., Showalter, M.R., 2012. The three-dimensional structure of Saturn's E ring. Icarus 217 (1), 322–338.

Hedman, M.M., Burns, J.A., Hamilton, D.P., Showalter, M.R., 2013. Of horseshoes and heliotropes: dynamics of dust in the Encke Gap. Icarus 223 (1), 252–276.

Hedman, M.M., Burt, J.A., Burns, J.A., Tiscareno, M.S., 2010. The shape and dynamics of a heliotropic dusty ringlet in the Cassini Division. Icarus 210 (1), 284–297.

Hedman, M.M., Cooper, N.J., Murray, C.D., Beurle, K., Evans, M.W., Tiscareno, M.S., Burns, J.A., 2010. Aegaeon (Saturn LIII), a G-ring object. Icarus 207 (1), 433–447.

Hedman, M.M., Murray, C.D., Cooper, N.J., Tiscareno, M.S., Beurle, K., Evans, M.W., Burns, J.A., 2009. Three tenuous rings/arcs for three tiny moons. Icarus 199 (2), 378–386.

Helled, R., Galanti, E., Kaspi, Y., 2015. Saturn's fast spin determined from its gravitational field and oblateness. Nature 520 (7), 202–204.

Horányi, M., 1996. Charged Dust Dynamics in the Solar System. Annu. Rev. Astron. Astrophys. 34 (1), 383–418.

Horányi, M., Burns, J.A., Hamilton, D.P., 1992. The dynamics of Saturn's E ring particles. Icarus 97 (2), 248–259.

Horányi, M., Juhász, A., Morfill, G.E., 2008. Large-scale structure of Saturn's E-ring. Geophys. Res. Lett. 35 (4), L04203.

Jacobson, R.A., Antreasian, P.G., Bordi, J.J., Criddle, K.E., Ionasescu, R., Jones, J.B., Mackenzie, R.A., Meek, M.C., Parcher, D., Pelletier, F.J., Owen Jr, W.M., Roth, D.C., Roundhill, I.M., Stauch, J.R., 2006. The gravity field of the Saturnian system from satellite observations and spacecraft tracking data. Astron. J. 132 (6), 2520–2526.

Johnson, R.E., Famá, M., Liu, M., Baragiola, R.A., Sittler, E.C., Smith, H.T., 2008. Sputtering of ice grains and icy satellites in Saturn's inner magnetosphere. Planet. Space Sci. 56 (9), 1238–1243.

Johnson, R.E., Luhmann, J.G., Tokar, R.L., Bouhram, M., Berthelier, J.J., Sittler, E.C., Cooper, J.F., Hill, T.W., Smith, H.T., Michael, M., Liu, M., Crary, F.J., Young, D.T., 2006. Production, ionization and redistribution of O_2 in Saturn's ring atmosphere. Icarus 180 (2), 393–402.

Juhász, A., Horányi, M., 2002. Saturn's E ring: a dynamical approach. J. Geophys. Res. 107 (A), 1066.

Juhász, A., Horányi, M., Morfill, G.E., 2007. Signatures of Enceladus in Saturn's E ring. Geophys. Res. Lett. 34 (9), L09104.

Kempf, S., Beckmann, U., Moragas-Klostermeyer, G., Postberg, F., Srama, R., Economou, T., Schmidt, J., Spahn, F., Grün, E., 2008. The E ring in the vicinity of Enceladus. I. Spatial distribution and properties of the ring particles. Icarus 193 (2), 420–437.

Krivov, A.V., Sremčević, M., Spahn, F., Dikarev, V.V., Kholshevnikov, K.V., 2003. Impact-generated dust clouds around planetary satellites: spherically symmetric case. Planet. Space Sci. 51 (3), 251–269.

Kurth, W.S., Averkamp, T.F., Gurnett, D.A., Wang, Z., 2006. Cassini RPWS observations of dust in Saturn's E ring. Planet. Space Sci. 54 (9), 988–998.

Lamy, L., Cecconi, B., Zarka, P., Canu, P., Schippers, P., Kurth, W.S., Mutel, R.L., Gurnett, D.A., Menietti, D., Louarn, P., 2011. Emission and propagation of Saturn kilometric radiation: magnetoionic modes, beaming pattern, and polarization state. J. Geophys. Res. 116 (A), A04212–n/a.

Münch, T., 2013. Dynamics and Charging of Dust in the Plasma Environment of Enceladus. University of Potsdam. Master's thesis

Murray, C.D., Dermott, S.F., 2000. Solar System Dynamics. Cambridge University Press, Queen Mary, University of London.

Northrop, T.G., Birmingham, T.J., 1990. Plasma drag on a dust grain due to coulomb collisions. Planet.. Space Sci. 38 (3), 319–326.

Porco, C.C., 2007. S/2007 S 4. IAU Circ. 8857, 2.

Roussos, E., Jones, G.H., Krupp, N., Paranicas, C., Mitchell, D.G., Krimigis, S.M., Woch, J., Lagg, A., Khurana, K., 2008. Energetic electron signatures of Saturn's smaller moons: evidence of an arc of material at Methone. Icarus 193 (2), 455–464.

Seiß, M., Srama, R., Sun, K.L., Seiler, M., Moragas-Klostermeyer, G., Kempf, S., Spahn, F., 2014. Pallene dust torus observations by the cosmic dust analyzer. Eur. Planet. Sci. Congr. 2014 9, EPSC2014–375.

Shannon, A., Mustill, A.J., Wyatt, M., 2015. Capture and evolution of dust in planetary mean-motion resonances: a fast, semi-analytic method for generating resonantly trapped disk images. Mon. Not. R. Astron. Soc. 448 (1), 684–702.

Sittler, E.C., Thomsen, M., Johnson, R.E., Hartle, R.E., Burger, M., Chornay, D., Shappirio, M.D., Simpson, D., Smith, H.T., Coates, A.J., Rymer, A.M., McComas, D.J., Young, D.T., Reisenfeld, D., Dougherty, M., Andre, N., 2006. Cassini observations of Saturn's inner plasmasphere: Saturn orbit insertion results. Planet. Space Sci. 54 (1), 1197–1210.

Spahn, F., Albers, N., Hörning, M., Kempf, S., Krivov, A.V., Makuch, M., Schmidt, J., Seiß, M., Miodrag, S., 2006. E ring dust sources: implications from Cassini's dust measurements. Planet. Space Sci. 54 (9–10), 1024–1032.

Spitale, J.N., Jacobson, R.A., Porco, C.C., Owen Jr, W.M., 2006. The orbits of Saturn's small satellites derived from combined historic and cassini imaging observations. Astron. J. 132 (2), 692–710.

Sun, K.-L., Schmidt, J., Spahn, F., 2015. Particle dynamics in the central ringlet of Saturn's Encke gap. arXiv1510.07730v1.

Thomas, P.C., Burns, J.A., Hedman, M., Helfenstein, P., Morrison, S., Tiscareno, M.S., Veverka, J., 2013. The inner small satellites of Saturn: a variety of worlds. Icarus 226 (1), 999–1019.

Tseng, W.L., Ip, W.H., Johnson, R.E., Cassidy, T.A., Elrod, M.K., 2010. The structure and time variability of the ring atmosphere and ionosphere. Icarus 206 (2), 382–389.

Verbiscer, A., French, R., Showalter, M., Helfenstein, P., 2007. Enceladus: cosmic graffiti artist caught in the act. Science 315 (5). 815–815

Verbiscer, A.J., Skrutskie, M.F., Hamilton, D.P., 2009. Saturn's largest ring. Nature 461, 1098–1100.

Vitense, C., Krivov, A.V., Kobayashi, H., Löhne, T., 2012. An improved model of the Edgeworth-Kuiper debris disk. Astron. Astrophys. 540, A30.

Wahlund, J., Bostrom, R., Gustafsson, G., Gurnett, D.A., Kurth, W.S., Averkamp, T., Hospodarsky, G.B., Persoon, A.M., Canu, P., Pedersen, A., Desch, M.D., Eriksson, A.I., Gill, R., Morooka, M.W., André, M., 2005. The inner magnetosphere of Saturn: Cassini RPWS cold plasma results from the first encounter. Geophys. Res. Lett. 32 (2), L20S09.

Wyatt, M.C., 2003. Resonant trapping of planetesimals by planet migration: Debris disk clumps and Vega's similarity to the solar system. Astron. J. 598 (2), 1321–1340.